AIAA JOURNAL
Vol. 44, No. 8, August 2006

Uncertainty Quantification with a B-Spline Stochastic Projection

Daniel R. Millman*
U.S. Air Force Flight Test Center, U.S. Air Force Test Pilot School, Edwards Air Force Base, California 93524
Paul I. King† and Raymond C. Maple‡
U.S. Air Force Institute of Technology, Wright–Patterson Air Force Base, Ohio 45433
Philip S. Beran§
U.S. Air Force Research Laboratory, Wright–Patterson Air Force Base, Ohio 45433
and
Lawrence K. Chilton‖
Air Force Institute of Technology, Wright–Patterson Air Force Base, Ohio 45433

DOI: 10.2514/1.11468

Presented is a new stochastic algorithm for computing the probability density functions and estimating bifurcations of nonlinear equations of motion whose system parameters are characterized by a Gaussian distribution. Polynomial and Fourier chaos expansions, which are spectral methods, have been used successfully to propagate parametric uncertainties in nonlinear systems. However, it is shown that bifurcations in the time domain are manifested as discontinuities in the stochastic domain, which are problematic for solution with these spectral approaches. Because of this, a new algorithm is introduced based on the stochastic projection method but employing a multivariate B spline. Samples are obtained by choosing nodes on the stochastic axes. These samples are used to build an interpolating function in the stochastic domain. Monte Carlo simulations are then very efficiently performed on this interpolating function to estimate probability density functions of a response. The results from this nonintrusive and non-Galerkin approach are in excellent agreement with Monte Carlo simulations of the governing equations, but at a computational cost 2 orders of magnitude less than a traditional Monte Carlo approach. The probability density functions obtained from the stochastic algorithm provide a rapid estimate of the probability of failure for a nonlinear pitch and plunge airfoil.

Nomenclature

a_h	=	distance from the airfoil midchord to the elastic axis, positive aft
$B_{i,k_{\xi_1},\boldsymbol{x}_{\xi_1}}$	=	the ith B spline of order k_{ξ_1} for the knot sequence $\boldsymbol{x}_{\xi_1}$
$B_{i,k_{\xi_2},\boldsymbol{x}_{\xi_2}}$	=	the jth B spline of order k_{ξ_2} for the knot sequence $\boldsymbol{x}_{\xi_2}$
b	=	airfoil midchord
C_l	=	lift coefficient
C_m	=	moment coefficient
c	=	airfoil chord
h	=	airfoil plunge
I_α	=	the second moment of inertia of the airfoil about the elastic axis, $mr_\alpha^2 b^2$
K_h	=	plunge stiffness of the airfoil, $m\omega_h^2$
K_α	=	torsional stiffness of the airfoil about the elastic axis, $I_\alpha \omega_\alpha^2$
k_{ξ_1}, k_{ξ_2}	=	order of the B splines on the ξ_1 and ξ_2 axes, respectively
m	=	mass of the airfoil
N_{ξ_1}, N_{ξ_2}	=	number of knots on the ξ_1 and ξ_2 axes, respectively
S_α	=	first moment of inertia of the airfoil about the elastic axis, $mx_\alpha b$
t	=	nondimensional time, scaled by V_∞ and b
V_r	=	reduced velocity, $V_\infty/(\omega_\alpha b)$
V_∞	=	freestream velocity
$w(\boldsymbol{\xi})$	=	Gaussian weight function
x_α	=	distance from the elastic axis to the center of mass of the airfoil, positive aft
$\boldsymbol{x}_{\xi_1}, \boldsymbol{x}_{\xi_2}$	=	vectors containing the knots on the ξ_1 and ξ_2 axes, respectively
α	=	airfoil pitch
β_α	=	airfoil cubic spring constant
γ_α	=	airfoil quintic spring constant
μ_s	=	airfoil mass ratio, $m/(\rho_\infty b^2 \pi)$
ξ_1, ξ_2	=	zero mean, unit variance Gaussian random variables
ρ_∞	=	freestream density
$\Psi(\boldsymbol{\xi})$	=	random basis functions
ω_r	=	frequency ratio, ω_h/ω_α
ω_α, ω_h	=	uncoupled natural frequencies in pitch and plunge, respectively

Superscripts

$\bar{}$	=	mean value
$\tilde{}$	=	standard deviation
$\hat{}$	=	expansion coefficient

Presented as Paper 1613 at the 45th AIAA/ASME/ASCE/AHS/ASC Sturctures, Structural Dynamics, and Materials Conference, Palm Springs, CA, 19–22 April 2004; received 10 June 2004; revision received 14 November 2005; accepted for publication 29 January 2006.

*Adjunct Assistant Professor, U.S. Air Force Institute of Technology. Senior Member.
†Professor, Department of Aeronautics and Astronautics. Senior Member.
‡Assistant Professor, Department of Aeronautics and Astronautics. Senior Member.
§Senior Research Aerospace Engineer, AFRL/VASD. Associate Fellow.
‖Associate Professor, Department of Mathematics and Statistics.

Introduction

FLUID-STRUCTURE interaction can result in the loss of dynamic stability to a time periodic instability that grows unbounded [1]. When nonlinear aerodynamics (e.g., transient shocks or boundary layer separation) or nonlinear structural responses are present to counter the growth of the unstable mode, the dynamic

response may stabilize to a limit cycle oscillation (LCO) [2–6].

To compute the dynamic response of an aeroelastic system, a time integration of the discrete aeroelastic equations is usually employed [3]. Because small variations in the system parameters can have a strong effect on the response [7], these equations are subsequently used in a Monte Carlo simulation (MCS) to quantify the effects of input uncertainty and estimate probability density functions (PDFs) of the responses. A full scale, high fidelity MCS solution can be prohibitive in terms of CPU time, and so a low fidelity modeling of the aerodynamics and structure is usually employed, but at a cost in predictive accuracy of the flowfield and structural response. Variational techniques [8] can reduce the effort of an MCS within a prescribed confidence level, but the number of realizations required to identify bifurcations can still be quite large [7].

Numerous approximate methods have been used to quantify uncertainty propagation, typically based upon a Galerkin's method [9–11]. An approximate method suited to nonlinear systems is reduced-order modeling (ROM), which represents a full order model with an optimal basis, in the mean square sense, through a Karhunen-Loeve expansion (KLE) [12–15]. ROM has the advantage that it can be efficiently tuned to capture flow physics at a high fidelity. Monte Carlo simulations are far more efficient on a reduced-order model than on the full order system, and these simulations can estimate responses about the mean that are useful in a multidisciplinary design [12]. However, the variations about the mean must be small in order for the ROM to remain valid.

A KLE cannot be used as an expansion when the response is not known a priori. The stochastic projection method [16–22] provides a way to build an expansion without knowing the form of the response. A random basis orthogonal with respect to the distribution of the input uncertainty is typically selected. When polynomials are selected as the basis, the method is referred to as a polynomial chaos expansion (PCE), where the word "chaos" is simply used to mean a basis of random variables [23]. Millman et al. [24] demonstrated that for limit cycle oscillations, a Fourier basis was more appropriate than a polynomial basis due to the behavior of bifurcations in the stochastic domain. With the Fourier basis orthogonalized with respect to the Gaussian PDF, this method was referred to as a Fourier chaos expansion (FCE). Regardless of the random basis chosen, denoted $\Psi_i(\boldsymbol{\xi})$, the deterministic coefficients of the expansion $\hat{\alpha}_i(t)$ are either computed as part of the time integration (intrusive approach) or estimated from a limited MCS (nonintrusive approach). The expansion of some response $\alpha(t, \boldsymbol{\xi})$ then takes the form [16,25]

$$\alpha(t, \boldsymbol{\xi}) = \sum_{i=0}^{P} \hat{\alpha}_i(t)\Psi_i(\boldsymbol{\xi}) \tag{1}$$

where the upper limit P is based on the order of the expansion and the number of input uncertainties, that is, the dimension d of $\boldsymbol{\xi}$. The vector $\boldsymbol{\xi}$ contains the random variables that characterize the uncertainty distribution of the input parameters. For a Gaussian distribution, the uncertainty of some input parameter β_α is characterized by its mean value $\bar{\beta}_\alpha$ and its standard deviation $\tilde{\beta}_\alpha$ as

$$\beta_\alpha = \bar{\beta}_\alpha + \xi_1\tilde{\beta}_\alpha \tag{2}$$

With the intrusive approach, the expansion in Eq. (1) is substituted directly into the governing equations of motion. For example, consider an equation of motion with the form

$$\mathcal{L}[\alpha(t)] + \beta_\alpha\alpha^3 = 0 \tag{3}$$

where $\mathcal{L}$ is a linear differential operator. Substituting Eqs. (1) and (2) into Eq. (3) yields

$$\mathcal{L}\left[\sum_{i=0}^{P}\hat{\alpha}_i\Psi_i\right] + \bar{\beta}_\alpha\sum_{i=0}^{P}\sum_{j=0}^{P}\sum_{k=0}^{P}\hat{\alpha}_i\hat{\alpha}_j\hat{\alpha}_k\Psi_i\Psi_j\Psi_k + \tilde{\beta}_\alpha\sum_{i=0}^{P}\sum_{j=0}^{P}\sum_{k=0}^{P}\hat{\alpha}_i\hat{\alpha}_j\hat{\alpha}_k\xi_1\Psi_i\Psi_j\Psi_k = 0 \tag{4}$$

To deal with expected values rather than random values, a Galerkin approach is employed. Equation (4) is multiplied by the basis Ψ_n and the Gaussian PDF w, which for d uncertainties is given by

$$w(\boldsymbol{\xi}) = \left(\frac{1}{\sqrt{2\pi}}\right)^d e^{-\frac{1}{2}\boldsymbol{\xi}^T\boldsymbol{\xi}} \tag{5}$$

to obtain

$$\mathcal{L}\left[\sum_{i=0}^{P}\sum_{n=0}^{P}\hat{\alpha}_i\Psi_i\Psi_n w\right] + \bar{\beta}_\alpha\sum_{i=0}^{P}\sum_{j=0}^{P}\sum_{k=0}^{P}\sum_{n=0}^{P}\hat{\alpha}_i\hat{\alpha}_j\hat{\alpha}_k\Psi_i\Psi_j\Psi_k\Psi_n w + \tilde{\beta}_\alpha\sum_{i=0}^{P}\sum_{j=0}^{P}\sum_{k=0}^{P}\sum_{n=0}^{P}\hat{\alpha}_i\hat{\alpha}_j\hat{\alpha}_k\xi_1\Psi_i\Psi_j\Psi_k\Psi_n w = 0 \tag{6}$$

Equation (6) is then integrated over the range of the Gaussian PDF w. The expected value operator for d uncertainty parameters is defined as

$$\langle f(\boldsymbol{\xi}), \Psi_n(\boldsymbol{\xi})\rangle = \int_{-\infty}^{\infty}\int_{-\infty}^{\infty}\cdots\int_{-\infty}^{\infty} f(\boldsymbol{\xi})\Psi_n(\boldsymbol{\xi})w(\boldsymbol{\xi})\,\mathrm{d}\xi_1\,\mathrm{d}\xi_2\cdots\mathrm{d}\xi_d \tag{7}$$

where $f(\boldsymbol{\xi})$ is any function of $\boldsymbol{\xi}$. By application of the expected value operator, Eq. (6) becomes

$$\mathcal{L}\left[\sum_{i=0}^{P}\sum_{n=0}^{P}\hat{\alpha}_i\langle\Psi_i, \Psi_n\rangle\right] + \bar{\beta}_\alpha\sum_{i=0}^{P}\sum_{j=0}^{P}\sum_{k=0}^{P}\hat{\alpha}_i\hat{\alpha}_j\hat{\alpha}_k\langle\Psi_i\Psi_j\Psi_k, \Psi_n\rangle + \tilde{\beta}_\alpha\sum_{i=0}^{P}\sum_{j=0}^{P}\sum_{k=0}^{P}\hat{\alpha}_i\hat{\alpha}_j\hat{\alpha}_k\langle\xi_1\Psi_i\Psi_j\Psi_k, \Psi_n\rangle = 0 \tag{8}$$

Because of the orthogonality of the basis Ψ_n with the Gaussian PDF w, the only terms that survive in the linear differential operator $\mathcal{L}$ are those where $i = n$. Thus the stochastic projection of the equation of motion given in Eq. (3) becomes a system of n equations which can be written as

$$\mathcal{L}[\hat{\alpha}_n] + \bar{\beta}_\alpha\sum_{i=0}^{P}\sum_{j=0}^{P}\sum_{k=0}^{P}\hat{\alpha}_i\hat{\alpha}_j\hat{\alpha}_k\frac{\langle\Psi_i\Psi_j\Psi_k, \Psi_n\rangle}{\langle\Psi_n, \Psi_n\rangle} + \tilde{\beta}_\alpha\sum_{i=0}^{P}\sum_{j=0}^{P}\sum_{k=0}^{P}\hat{\alpha}_i\hat{\alpha}_j\hat{\alpha}_k\frac{\langle\xi_1\Psi_i\Psi_j\Psi_k, \Psi_n\rangle}{\langle\Psi_n, \Psi_n\rangle} = 0 \tag{9}$$

The condition of orthogonality with respect to the Gaussian PDF substantially reduces the number of nonzero expected values for a linear problem. As nonlinearity increases, the number of nonzero terms grows rapidly due to the coupling evident in Eq. (9). Computational efficiency is rapidly lost when high order expansions of highly nonlinear equations are required [24,26–29].

To gain back some efficiency, researchers have employed the nonintrusive approach. A limited MCS is performed and the samples obtained are used to estimate the coefficients. Because of the random selection of samples, the expected value operator is again employed. The coefficients are estimated from [30]

$$\hat{\alpha}_i = \frac{\langle\alpha, \Psi_i\rangle}{\langle\Psi_n, \Psi_n\rangle} \tag{10}$$

This nonintrusive approach substantially reduces the number of expected values that need to be precomputed and stored. High order expansions are still required to capture behavior in the vicinity of a bifurcation.

Finding a proper basis to capture bifurcations in the stochastic domain is an active area of research. Notably, Le Maître et al. [31,32] have employed wavelets in an intrusive expansion to better capture discontinuous behavior in the stochastic domain. This paper examines a nonspectral stochastic algorithm, based on the stochastic projection method. This research builds on the results reported by Millman et al. [24] by gaining a better understanding of the stochastic projections themselves. These projections are shown to include piecewise continuous functions for problems involving bifurcations.

An efficient method for approximating these projections is to obtain samples of the response over a specified interval of the stochastic axes (nonintrusive approach). These samples need not be obtained by a limited MCS, eliminating the need for computing and storing expected values (non-Galerkin). A surface in the stochastic domain is fit to those samples with a multivariate basis spline (B spline). This interpolating surface is then used to perform the MCS needed to approximate the PDFs. These approximate PDFs provide an estimate of the bifurcation behavior of the governing equations. The utility of this algorithm is demonstrated by examining the LCO response and predicting the probability of failure of a nonlinear pitch and plunge airfoil.

Pitch and Plunge Airfoil

The 2 degrees of freedom pitch and plunge airfoil is depicted in Fig. 1. A nonlinear structural response is modeled through the following equations of motion [1,3]:

$$m\ddot{h} + S_\alpha \ddot{\alpha} + K_h h = -\tfrac{1}{2}\rho_\infty V_\infty^2 c C_l(t) \tag{11}$$

$$S_\alpha \ddot{h} + I_\alpha \ddot{\alpha} + K_\alpha(\alpha + \beta_\alpha \alpha^3 + \gamma_\alpha \alpha^5) = \tfrac{1}{2}\rho_\infty V_\infty^2 c^2 C_m(t) \tag{12}$$

where $C_l(t)$ is the lift coefficient taken positive down and $C_m(t)$ is the moment coefficient taken positive nose up about the elastic axis. After nondimensionalizing, Eqs. (13) and (14) become

$$\ddot{h} + x_\alpha \ddot{\alpha} + \left(\frac{\omega_r}{V_r}\right)^2 h = -\frac{C_l(t)}{\pi \mu_s} \tag{13}$$

$$\frac{x_\alpha}{r_\alpha^2}\ddot{h} + \ddot{\alpha} + \frac{1}{V_r^2}(\alpha + \beta_\alpha \alpha^3 + \gamma_\alpha \alpha^5) = \frac{2C_m(t)}{\pi \mu_s r_\alpha^2} \tag{14}$$

where it is understood that the plunge h in Eqs. (13) and (14) has been nondimensionalized with respect to the semichord. To integrate the above equations, an aerodynamic model is needed to provide the lift and moment coefficients as a function of time. Following Lee et al. [3] the coefficients are obtained from an incompressible flow model given by Fung [1]. With this incompressible flow model, Eqs. (13) and (14) can be rewritten as a set of eight first order differential equations. The details of the derivation are given by Lee et al. [3].

The following parameters were chosen for this model problem:

$$\mu_s = 100 \qquad a_h = -0.5 \qquad x_\alpha = 0.25 \qquad \omega_r = 0.2$$
$$\gamma_\alpha = 20 \qquad r_\alpha = -0.5$$

A Gaussian distribution was assumed for the cubic spring constant β_α and the initial pitch $\alpha(0)$, that is,

$$\beta_\alpha = \bar{\beta}_\alpha + \xi_1 \tilde{\beta}_\alpha \tag{15}$$

$$\alpha(0) = \bar{\alpha}(0) + \xi_2 \tilde{\alpha}(0) \tag{16}$$

A mean value of $\bar{\alpha}(0) = 0.0$ and a standard deviation of $\tilde{\alpha}(0) = 0.2$ were used. The standard deviation of the cubic spring constant was $\tilde{\beta}_\alpha = 0.3$.

Two cases are considered for the mean value of the cubic spring constant. The first is for a positive value with $\bar{\beta}_\alpha = 3$ (hard spring), and the second is for a negative value with $\bar{\beta}_\alpha = -3$ (soft spring). As evident from Eq. (12), a hard spring further stabilizes the structure in pitch whereas a soft spring destabilizes the structure. Thus, the two values of β_α lead to dramatically different responses. γ_α is always positive and always stabilizes the structure, although its influence is felt for only large amplitudes in pitch. An analysis of the deterministic governing equations ($\tilde{\beta}_\alpha = 0.0$) yields a Hopf bifurcation point at $V_r = 6.279$, where the Hopf bifurcation point is defined as the critical point that connects a dynamically stable stationary (no motion) solution to a stable periodic motion [33]. For a hard spring, as the reduced velocity is increased, the amplitude of the LCO increases monotonically from the Hopf bifurcation point. This is a supercritical response and labeled with $\beta_\alpha = 3.0$ in Fig. 2. For a soft spring, a large amplitude excursion can lead to a LCO below the Hopf bifurcation point. A small amplitude excursion below the Hopf bifurcation point will decay to the dynamically stable stationary solution. This is a subcritical response with a turning point [33], as shown in Fig. 2. Note that with $\beta_\alpha = -3$, LCOs are obtained at a reduced velocity as low as $V_r = 5.902$.

When the uncertainties (ξ_1 and ξ_2) are included, the amplitude of the LCO varies for a given reduced velocity. Probability density functions for both the hard and soft springs are shown in Figs. 3a and 3b for a range of reduced velocities. These PDFs were obtained from a four thousand run MCS at each reduced velocity, where the time integrations were carried out far enough ($t_{\max} \geq 2000$) to ensure each simulation achieved a fully developed LCO. It should be noted that the PDFs are approximated from the four thousand samples through a Parzen-window approach [34]. Figures 4a and 4b depict bifurcation diagrams that summarize the results of the PDFs for both the supercritical and subcritical responses. In these figures, the range of peak and secondary responses represent the envelope of scatter values about the average peak response.

Linear aerodynamics predicts a flutter point, which is coincident with the Hopf bifurcation point. That is, the flutter point is the loss of linear stability. Typically, through linear analysis or flight test, flutter points are determined and aircraft speeds are placarded so as to avoid flight above the flutter point. The subcritical response illustrated in Fig. 4 can lead to LCO below the classically defined flutter point. This represents a risk to an aircraft as the aircraft can exhibit large oscillations below the placard speed determined by the flutter point. For this study, the probability of failure for the airfoil was defined as

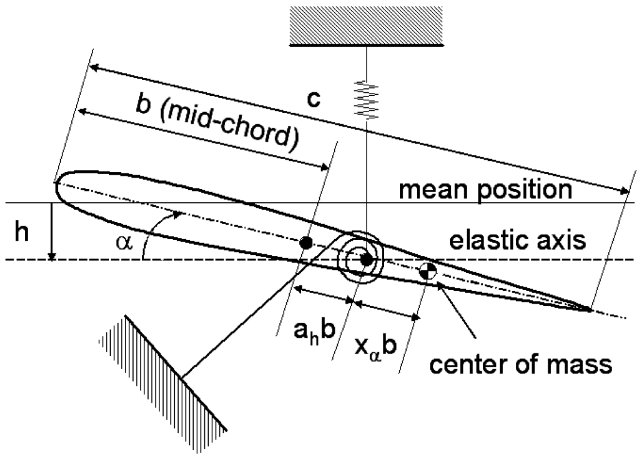

Fig. 1 The pitch and plunge airfoil.

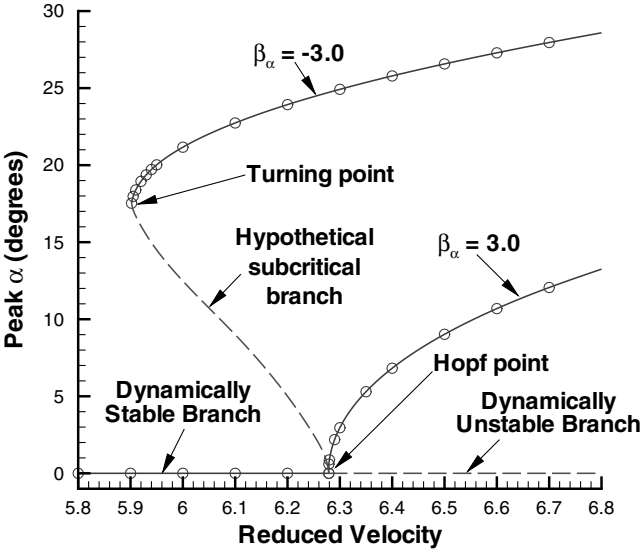

Fig. 2 Bifurcation diagram.

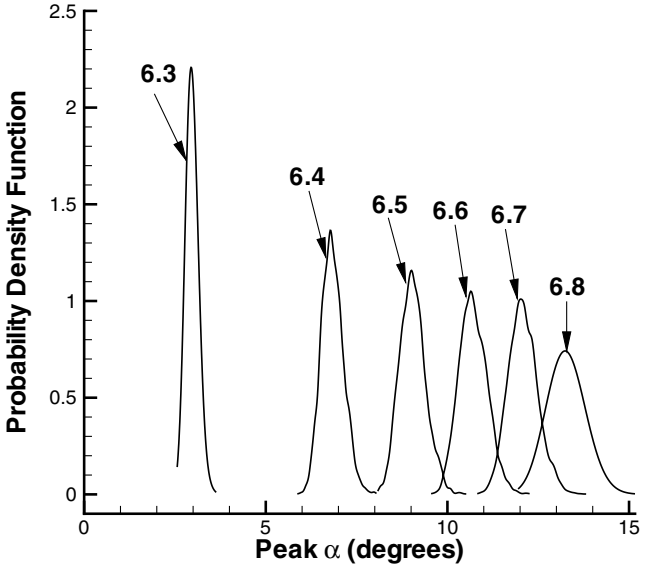

a) Hard spring

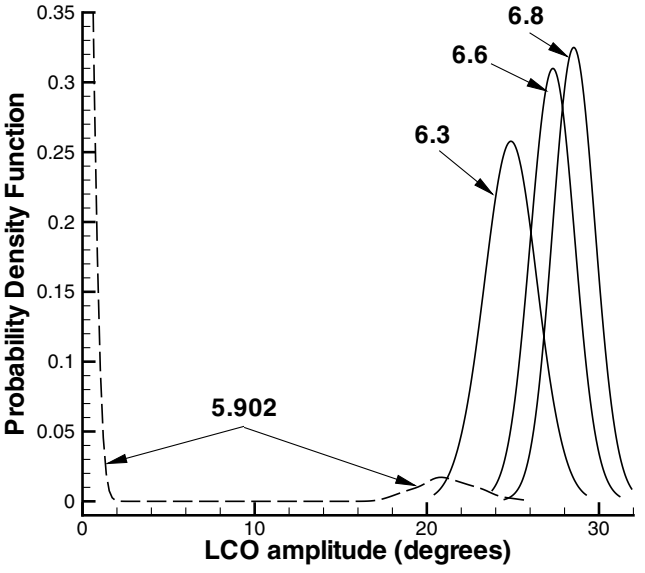

b) Soft spring

Fig. 3 Probability density functions at various reduced velocities. Numbers indicate reduced velocity.

pitch amplitudes exceeding 3 deg while in LCO. The PDFs obtained from the subcritical response can then predict the probability of failure for the airfoil example given above. Figure 5 shows the probability of failure for the subcritical case. Note that as the cubic spring constant varies, the location of the turning point bifurcation changes, leading to LCO as low as $V_r \approx 5.70$.

Stochastic Projection

A stochastic projection is a projection of the system response onto the space covered by the basis functions in the random variables. Typically this projection is obtained at a specific instance in time. For a time domain analysis, at a very large time, these projections can become so complicated (nonlinear, discontinuous) in form that even a very large order expansion cannot capture the shape of the projection [29]. Beran et al. [30] circumvent this issue with the nonintrusive PCE approach. The nonintrusive PCE approach essentially removes the time dependency by obtaining samples of the LCO response once the LCO is fully developed. Beran's results were obtained from an efficient cyclic approach, not involving a time domain analysis [30]. This present work examines the stochastic projections from a time domain approach.

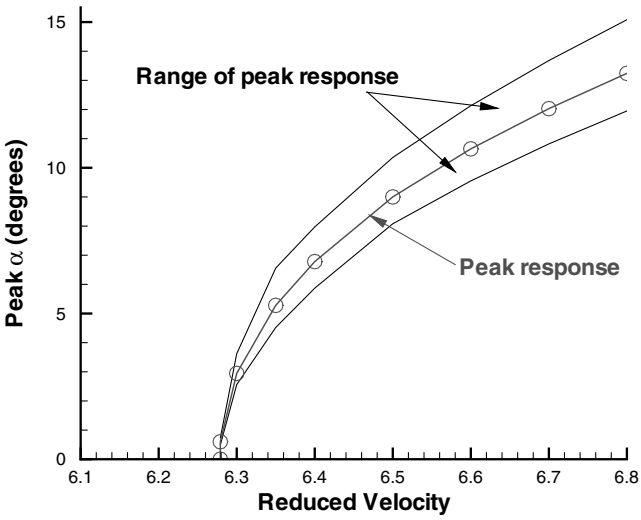

a) Hard spring

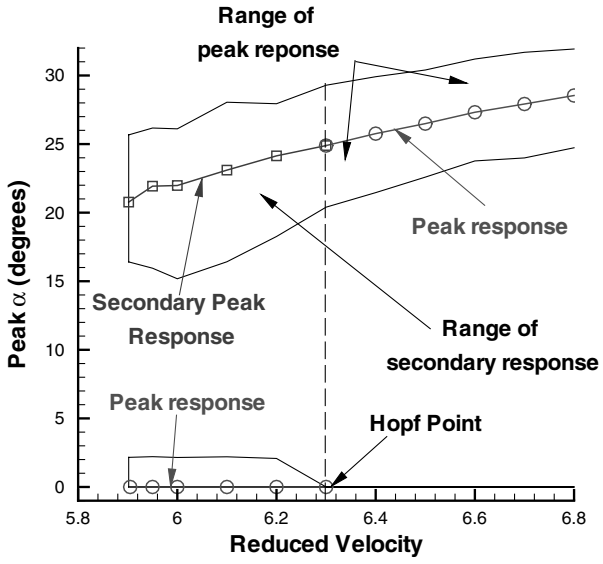

b) Soft spring

Fig. 4 Bifurcation diagrams with the inclusion of uncertainties.

To better understand the behavior of the stochastic projections, two projections are plotted in Fig. 6. These projections were obtained from a four thousand MCS on the hard spring system at $V_r = 6.5$, and sorted with respect to each random variable. In Fig. 6a, the stochastic projection of the response, peak α, with respect to the uncertainty in the cubic spring constant, ξ_1 is a smooth continuous function. The same initial pitch $\alpha(0)$ was used for each simulation. A nonzero value was chosen to ensure an LCO developed. In Fig. 6b, the four thousand run MCS was repeated, but this time the cubic spring constant was deterministic and the initial pitch was uncertain. Again, the stochastic projection with respect to the uncertainty in the initial pitch, appears to be a smooth continuous function, but a singular point exists at $\xi_2 = 0$. This singularity corresponds to the dynamically unstable equilibrium branch on the bifurcation diagram (Fig. 4).

The stochastic projections for the soft spring at $V_r = 6.2$ are shown in Fig. 7. In Fig. 7a, a very large initial amplitude was chosen for each simulation to ensure LCO was achieved. Again, the stochastic projection with respect to the uncertainty in the cubic spring constant is a smooth, continuous function. However, the stochastic projection with respect to the uncertainty in the initial pitch, Fig. 7b, is a piecewise continuous function. The discontinuities are a manifestation of the subcritical branch in the bifurcation diagram. Above a certain absolute value in initial pitch, an LCO develops. Below this absolute value in initial pitch, a dynamically stable solution is achieved. The nonintrusive PCE approach, or

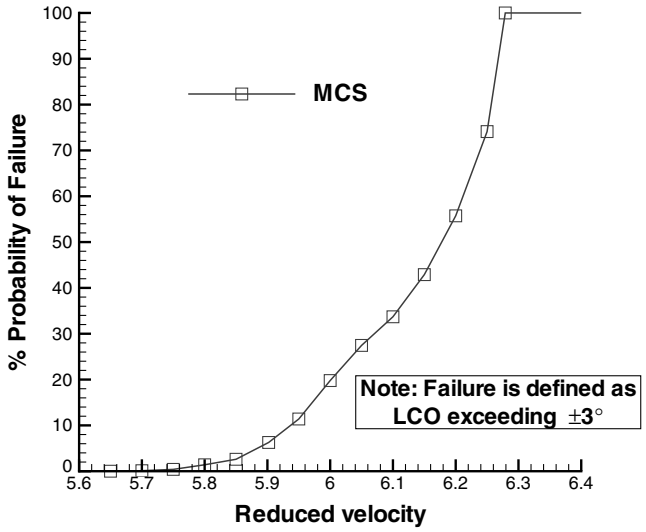

Fig. 5 Airfoil probability of failure.

indeed any spectral approach, would be a poor choice in attempting to approximate this particular projection.

Given that the stochastic projections can be piecewise continuous over the interval of interest, splines are appropriate functions for approximating these projections. An important property of the multivariate B splines chosen for this work is that they are a compact support basis. That is, the influence of any particular B spline coefficient extends over a few intervals [35]. The practical importance of this property is that oscillations in the vicinity of discontinuities can be avoided with the proper choice in the order, k_{ξ_1} or k_{ξ_2}, of the B spline. The order used in this work is $k_{\xi_1} = k_{\xi_2} = 2$, which is equivalent to a piecewise linear interpolation [35]. The expansion of the univariate B splines for ξ_1 and ξ_2 are given by

$$\alpha(\xi_1) = \sum_{i=1}^{N_{\xi_1}} \hat{\alpha}_{i,\xi_1} B_{i,k_{\xi_1},\boldsymbol{x}_{\xi_1}}(\xi_1) \tag{17}$$

$$\alpha(\xi_2) = \sum_{j=1}^{N_{\xi_2}} \hat{\alpha}_{j,\xi_2} B_{j,k_{\xi_2},\boldsymbol{x}_{\xi_2}}(\xi_2) \tag{18}$$

where $\boldsymbol{x}_{\xi_1}$ is the vector of N_{ξ_1} knots on the ξ_1 axis and $\boldsymbol{x}_{\xi_2}$ is the vector of N_{ξ_2} knots on the ξ_2 axis. The multivariate B spline is the tensor product of the two univariate B splines and can be explicitly written as [35]

$$\alpha(\xi_1, \xi_2) = \sum_{i=1}^{N_{\xi_1}} \sum_{j=1}^{N_{\xi_2}} \hat{\alpha}_{ij} B_{j,k_{\xi_2},\boldsymbol{x}_{\xi_2}}(\xi_2) B_{i,k_{\xi_1},\boldsymbol{x}_{\xi_1}}(\xi_1) \tag{19}$$

The coefficient matrix, made up of the elements $\hat{\alpha}_{ij}$, is solved by repeated evaluations of the univariate spline interpolation problem, the details of which are given in de Boor [35].

Now an efficient stochastic algorithm that is robust enough to identify bifurcations can be described. First, an interval is chosen in the stochastic domain over which samples of the LCO response (peak α) will be obtained. Next, the location of nodes to be sampled in that interval is determined. The multivariate B spline that approximates the response surface in the stochastic domain is then determined. Finally, an MCS is performed on this response surface to estimate the PDF of the response.

The interval selected is based on the distribution of random variables. For this work, the random variables have a Gaussian distribution. Strictly speaking, the interval defined for a Gaussian random variable is the whole real line. There is, however, a practical limit to this interval. The random variables control parametric uncertainties and these parameters must be kept within specified bounds in order for the equations of motion to be numerically well behaved. In a real world application the mean and standard deviation may be dictated by manufacturing, instrument error, or physical

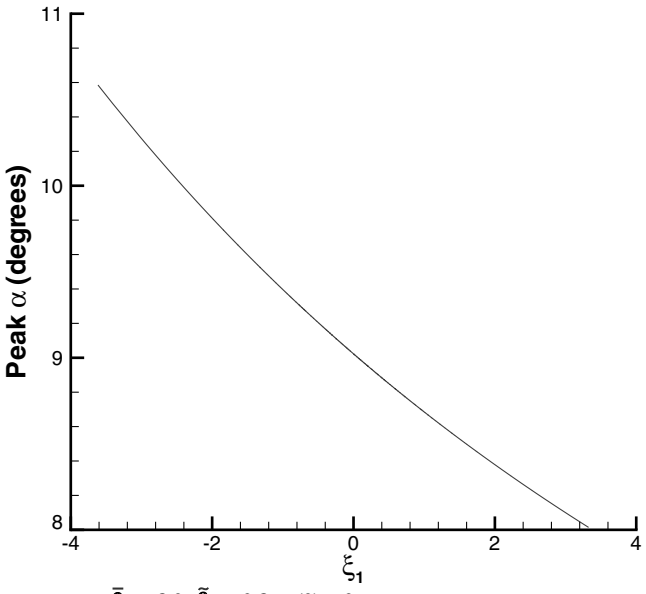

a) $V_r = 6.5$, $\bar{\beta}_\alpha = 3.0$, $\tilde{\beta}_\alpha = 0.3$, $\alpha(0) > 0$

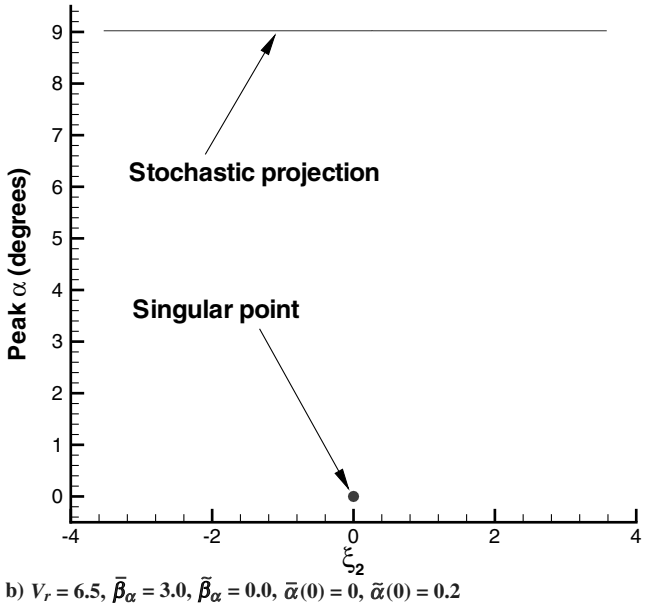

b) $V_r = 6.5$, $\bar{\beta}_\alpha = 3.0$, $\tilde{\beta}_\alpha = 0.0$, $\bar{\alpha}(0) = 0$, $\tilde{\alpha}(0) = 0.2$

Fig. 6 Stochastic projection of peak α response onto the random variables ξ_1 and ξ_2 (hard spring).

phenomena such as wind gusts. For this model problem the mean and standard deviation were selected to illustrate supercritical and subcritical responses. It was found that for the large standard deviation chosen in pitch, $\tilde{\alpha}(0) = 0.2$ radians, the model became unstable for large values of ξ_2 ($\xi_2 > 4$). Because

$$\left(\frac{1}{\sqrt{2\pi}}\right)^2 \int_{-4}^{4}\int_{-4}^{4} e^{-(1/2)(\xi_1^2+\xi_2^2)}\, \mathrm{d}\xi_1\, \mathrm{d}\xi_2 \approx 0.9999 \tag{20}$$

99.99% of all responses occur on the interval $[-4, 4]$ in both stochastic axes. Thus, this was the interval selected for both ξ_1 and ξ_2.

With the interval selected, nodes along the stochastic axis must be chosen that will efficiently capture the desired projection. Here again a compromise is achieved. In order for the B spline to be valid over the entire interval, nodes must be selected that span the entire interval. However, a Gaussian distribution of the nodes would cluster all the nodes near the mean value, leaving a large gap between the nodes and the endpoints of the interval. Nodes at ± 4 are required to span the interval. Nodes at ± 2.5 are added to bridge the gap between the Gaussian spaced nodes and the endpoints of the interval. The Gaussian spaced nodes are determined by integration of the Gaussian

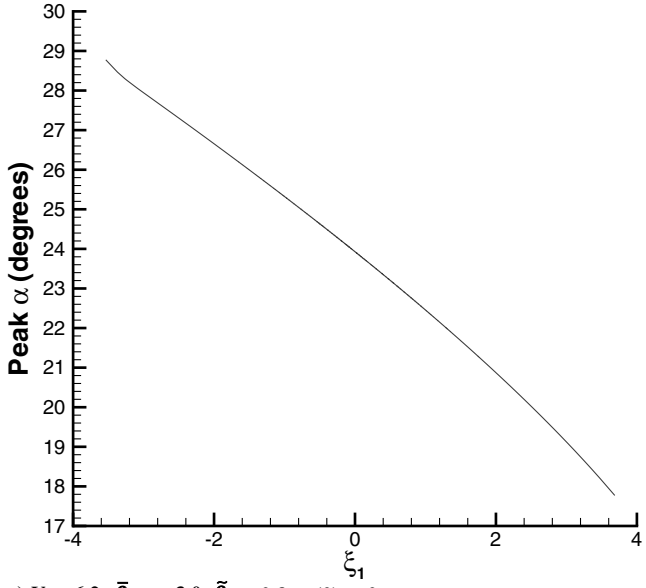

a) $V_r = 6.2$, $\bar{\beta}_\alpha = -3.0$, $\tilde{\beta}_\alpha = 0.3$, $\alpha(0) \gg 0$

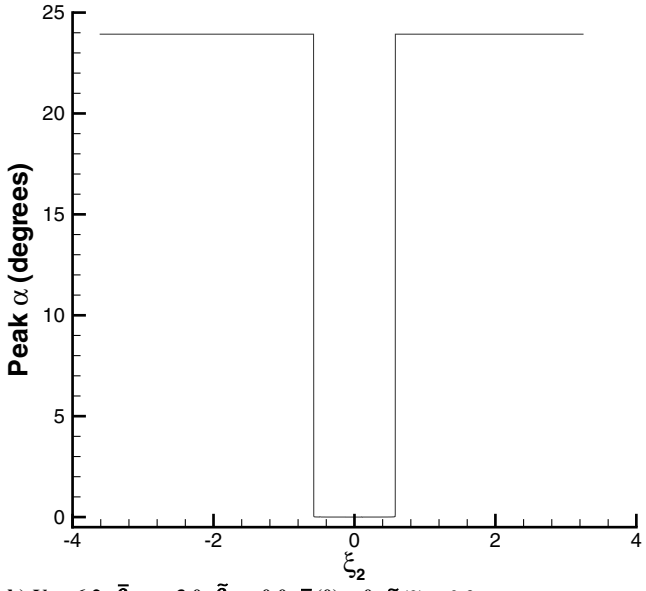

b) $V_r = 6.2$, $\bar{\beta}_\alpha = -3.0$, $\tilde{\beta}_\alpha = 0.0$, $\bar{\alpha}(0) = 0$, $\tilde{\alpha}(0) = 0.2$

Fig. 7 Stochastic projection of peak α response onto the random variables ξ_1 and ξ_2 (soft spring).

PDF, $w(\xi_1)$ or $w(\xi_2)$ [Eq. (5) with $d = 1$]. That is, the nodes are determined in one dimension and the same nodes are used in the other dimension. The determination of the nodes proceeds as follows. Some number of nodes are selected on the interval [0,4]. Let this number of nodes be represented by I along the ξ_1 axis and J along ξ_2 axis. Noting that

$$\int_0^4 \frac{1}{\sqrt{2\pi}} e^{-\frac{1}{2}\xi_1^2} \, \mathrm{d}\xi_1 \approx \frac{1}{2} \tag{21}$$

the remaining nodes are selected based on equal intervals of the probabilities. For example, with $I = 2$ and one node fixed at $\xi_1 = 4$, the second node is determined from

$$\int_0^a \frac{1}{\sqrt{2\pi}} e^{-\frac{1}{2}\xi_1^2} \, \mathrm{d}\xi_1 = \frac{1}{4} \tag{22}$$

where a is the location of the node. A simple search leads to a value of $a = 0.67449$. Proceeding in a like manner for $I = 4$ and $I = 8$ leads to the node values given in Table 1. Because of the symmetry of the nodes and the extra nodes at $\xi_1 = \pm 2.5$, the total number of nodes along the ξ_1 stochastic axis is given by $2I + 2$.

Table 1 Gaussian distributed nodes

$I = 2$	$I = 4$	$I = 8$
——	——	±0.15731
——	±0.31864	±0.31684
——	——	±0.48878
±0.67449	±0.67449	±0.67449
——	——	±0.88715
——	±1.15035	±1.15035
——	——	±1.53412
±2.5	±2.5	±2.5
±4.0	±4.0	±4.0

Samples of the response are obtained at the selected values of ξ_1 and ξ_2. From these samples, the multivariate B-spline problem can be solved for the coefficient matrix, $\hat{\alpha}_{ij}$ in Eq. (19). After these coefficients are determined, an MCS is performed on Eq. (19). This MCS is extremely efficient, as is demonstrated in the next section.

This algorithm fits into the stochastic projection framework through the following derivation, which parallels the development given by Eqs. (3–12). Consider the set of nodes $\boldsymbol{x}$ such that $x_i \in [-a, a]$ and $x_1 = -a < x_2 < \cdots < x_I = a$ for some integer I. Because it was noted that the above algorithm is a piecewise linear interpolation, the appropriate basis for expansion would be the hat function, which has the property [35]

$$\Psi_j(x_i) = \delta_{ij} \tag{23}$$

where δ_{ij} is the Dirac delta function. Additionally, $\delta_j(x) = \delta(x - x_j)$, which indicates sampling at a node. Just as the expected value operator was defined in Eq. (7) in order to integrate out the random variables, similar inner products with the trial basis δ_j and the weight function $w(x) = 1$ can be developed and are given by

$$\langle \Psi_i, \delta_j \rangle = \int_{-a}^{a} \Psi_i(x)\delta(x - x_j) \, \mathrm{d}x = \Psi_i(x_j) = \delta_{ij} \tag{24}$$

$$\langle x\Psi_i, \delta_j \rangle = \int_{-a}^{a} x\Psi_i(x)\delta(x - x_j) \, \mathrm{d}x = x_j\Psi_i(x_j) = x_j\delta_{ij} \tag{25}$$

The piecewise linear approximation to the response $\alpha(t, x)$ becomes

$$\alpha(t, x) = \sum_{i=1}^{I} \hat{\alpha}_i(t)\Psi_i(x) \tag{26}$$

and can be substituted into Eq. (3). By performing the stochastic projection and making use of the above inner products, the following system of equations results:

$$\mathcal{L}[\hat{\alpha}_j] + (\bar{\beta}_\alpha + x_j\tilde{\beta}_\alpha)\hat{\alpha}_j^3 = 0 \tag{27}$$

Thus, the samples of the random variable are used to obtain samples of the response and a piecewise linear approximation to the response is obtained from the B splines. While the PCE method provides a best fit to the stochastic projection and converges, in the mean square sense, to an MCS [36], the piecewise linear interpolation is exact at the nodes and, with a sufficient number of nodes, is a nearly optimal fit to an MCS [35].

Results

The hard spring is examined first. Setting $I = 2$ and holding the initial pitch constant at some value greater than zero, samples are obtained along the ξ_1 axis at $V_r = 6.5$. The univariate spline, Eq. (17) is solved for the coefficients $\hat{\alpha}_{i,\xi_1}$. This equation is then used in an MCS to produce the stochastic projection in Fig. 8a. Setting $J = 2$ and holding the cubic spring constant at $\beta_\alpha = 3.0$, the same procedure was used to determine the coefficients $\hat{\alpha}_{i,\xi_2}$ in Eq. (18). An MCS on Eq. (18) produces the stochastic projection shown in Fig. 8b. These projections are in excellent agreement with the projections shown in Fig. 6. This should be expected because the projections are linear or very nearly linear across the respective intervals.

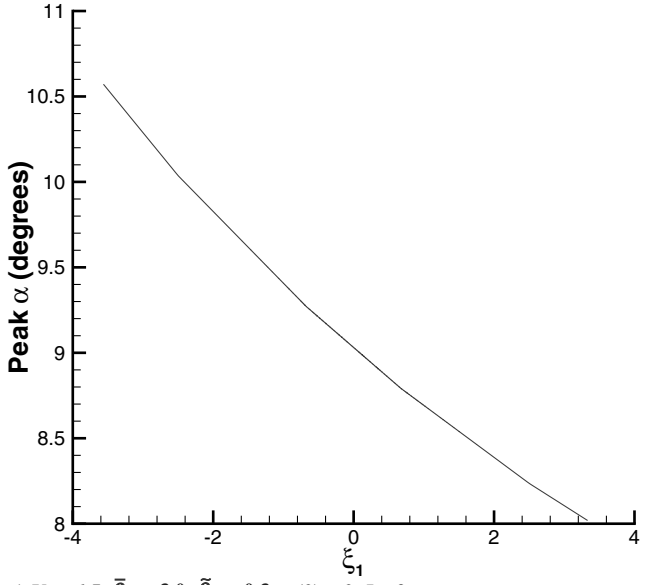

a) $V_r = 6.5$, $\bar{\beta}_\alpha = 3.0$, $\tilde{\beta}_\alpha = 0.3$, $\alpha(0) > 0$, $I = 2$

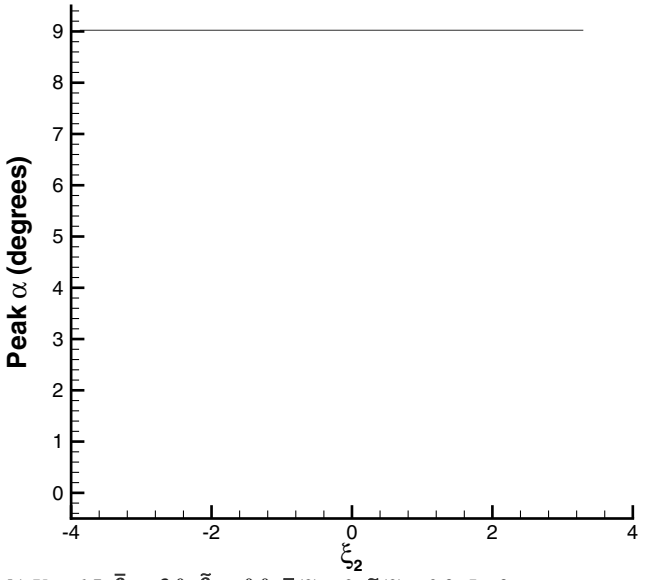

b) $V_r = 6.5$, $\bar{\beta}_\alpha = 3.0$, $\tilde{\beta}_\alpha = 0.0$, $\bar{\alpha}(0) = 0$, $\tilde{\alpha}(0) = 0.2$, $J = 2$

Fig. 8 Stochastic projection of peak α response onto the random variables ξ_1 and ξ_2 (hard spring).

Allowing both the cubic spring constant and the initial pitch to be uncertain and setting $I = 2$ and $J = 2$, thirty-six samples are obtained. After the coefficients in Eq. (19) are determined, an MCS is performed on this equation. The PDF of the response is computed and compared with the PDF from the MCS on the governing equations. The agreement between the two PDFs is excellent, as shown in Fig. 9. Again this should be expected due to the smoothness of the approximated functions. The efficiency of obtaining samples of the response, solving the multivariate B-spline problem, and performing an MCS on Eq. (19) is 2 orders of magnitude faster than performing an MCS on the governing equations.

The soft spring case is examined at $V_r = 6.2$. The stochastic projection in Fig. 10a is obtained as before with the soft spring uncertain and the initial pitch constant at a large, nonzero value. The stochastic projection in Fig. 10b is obtained keeping the soft spring constant and allowing the initial pitch to be uncertain. The projection with respect to ξ_1 required $I = 4$ (10 samples) to obtain the proper curvature. The projection with respect to ξ_2 required $J = 8$ to obtain a good approximation to the discontinuities. These stochastic projections compare well with those in Fig. 7.

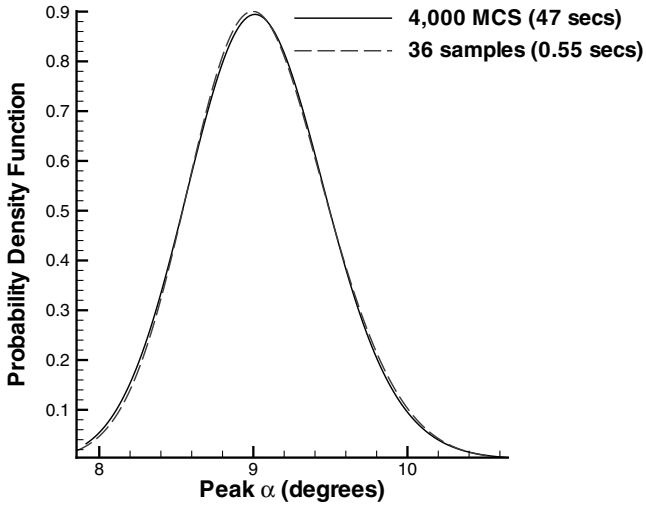

Fig. 9 PDF comparisons for the hard spring.

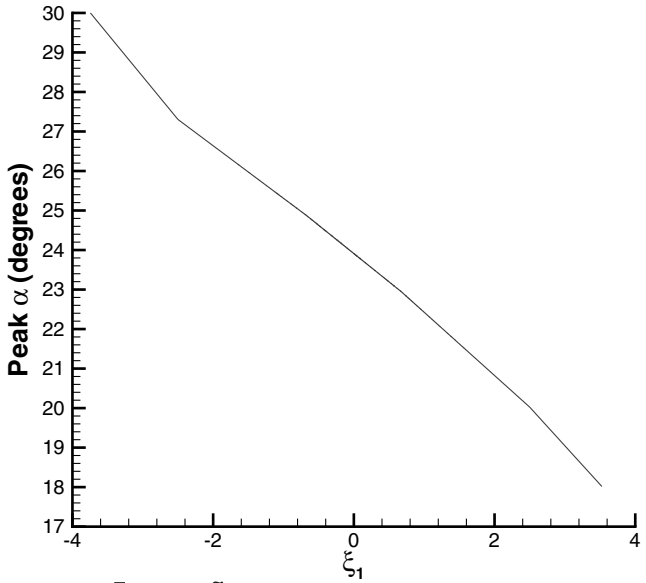

a) $V_r = 6.2$, $\bar{\beta}_\alpha = -3.0$, $\tilde{\beta}_\alpha = 0.3$, $\alpha(0) \gg 0$, $I = 4$

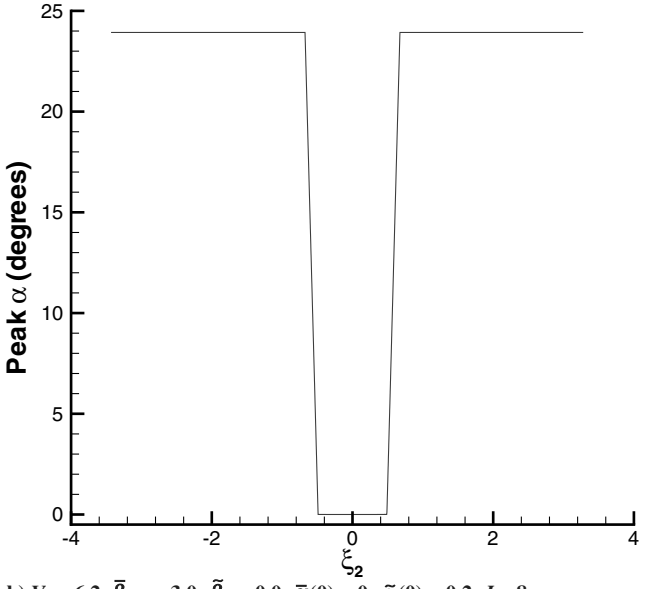

b) $V_r = 6.2$, $\bar{\beta}_\alpha = -3.0$, $\tilde{\beta}_\alpha = 0.0$, $\bar{\alpha}(0) = 0$, $\tilde{\alpha}(0) = 0.2$, $J = 8$

Fig. 10 Stochastic projection of peak α response onto the random variables ξ_1 and ξ_2 (soft spring).

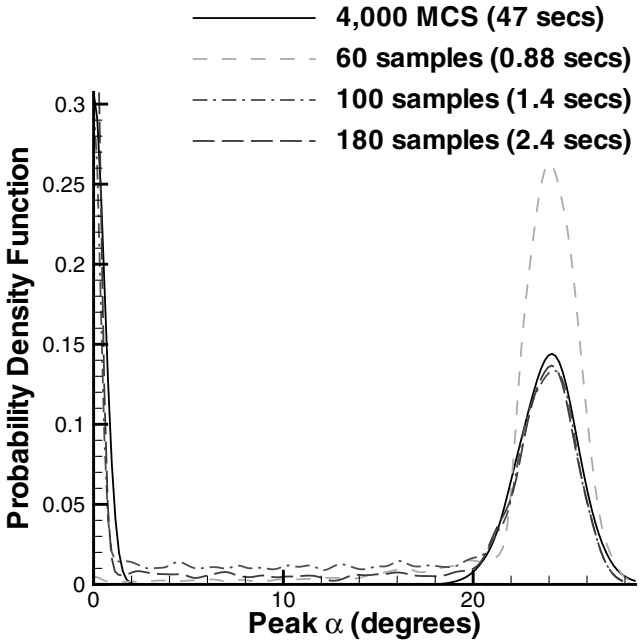

Fig. 11 PDF comparisons for the soft spring.

Again allowing both the cubic spring constant and the initial pitch to be uncertain, PDFs were obtained from the stochastic projection method with $I = 4$ and $J = 2$, 4, and 8 (60, 100, and 180 samples, respectively). These PDFs are compared with the PDF from the MCS and are shown in Fig. 11. As the number of nodes increase along the ξ_2 axis, agreement with the PDF obtained from the MCS improves rapidly. The PDF with $J = 4$, is already in excellent agreement with the MCS results. With $J = 8$, the steeper slope in the approximation of the discontinuities manifests itself as fewer realizations between the peak and secondary responses (a better bimodal approximation).

With the stochastic algorithm verified for the above cases, bifurcation diagrams with the inclusion of uncertainties are now developed. For the hard spring, PDFs were obtained over the same range of reduced velocities as for the MCSs. Setting $I = J = 2$ was sufficient for these cases because all the responses were supercritical. For the soft spring, the PDFs below the Hopf bifurcation point were obtained with $I = 4$ and $J = 8$, because these responses were subcritical. Above the Hopf point, once again $I = J = 2$ was sufficient. These PDFs were then used to build the bifurcation diagrams shown in Fig. 12. The agreement between these bifurcation diagrams and the ones shown in Fig. 4 is excellent. The peak (or secondary peak) responses from the stochastic projection method are within 1–2% of the peak (or secondary peak) responses from the MCS. The variation of peak (or secondary peak) responses are well within 5% of the variation given by the MCS. The time required to build these bifurcation diagrams was approximately 2 orders of magnitude less than with a traditional MCS approach.

From the subcritical responses, an estimate of the probability of failure could be obtained. Defining the probability of failure as the LCO in pitch exceeding three degrees, a comparison between the MCS prediction and the B-spline prediction is shown in Fig. 13. Errors were introduced at the discontinuities because the selected nodes were not coincident with the locations of the discontinuities. These errors led to a conservative estimate in the probability of failure, as seen in Table 2. Each failure estimate from the MCS required approximately ten minutes of computer time, whereas each estimate from the stochastic algorithm required approximately three seconds.

Conclusion

A very efficient algorithm for determining the propagation of uncertainties in a highly nonlinear system has been presented. The nonlinear system examined was a pitch and plunge airfoil with cubic

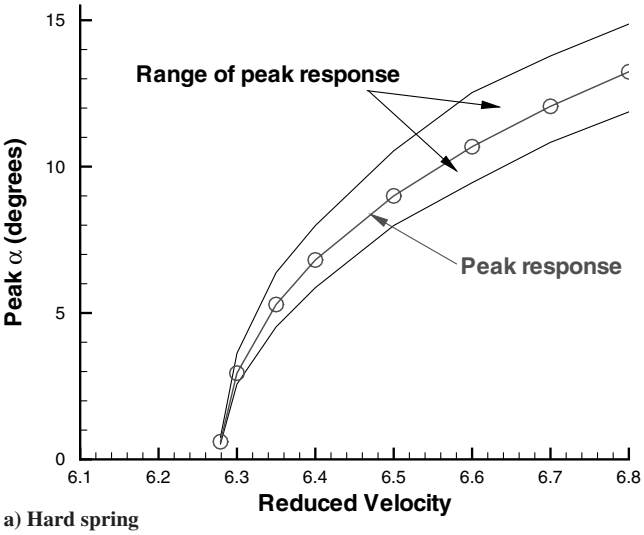

a) Hard spring

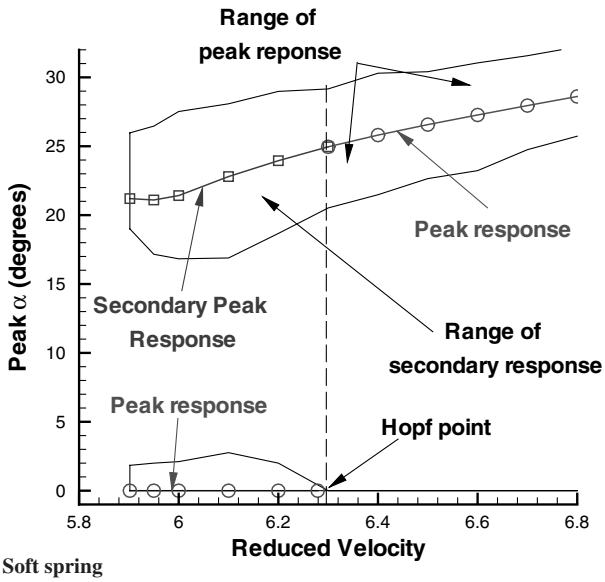

b) Soft spring

Fig. 12 Bifurcation diagrams built with the stochastic projection method.

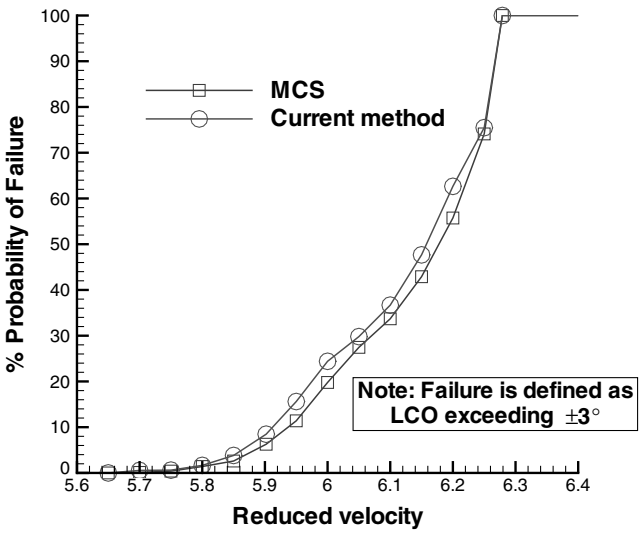

Fig. 13 Comparison of probability of failure predictions with MCS and B-spline algorithm.

Table 2 Estimates for the probability of failure

Reduced velocity (V_r)	MCS (%)	Stochastic algorithm (%)	Difference (%)
5.70	0.11	0.55	0.44
5.75	0.40	0.61	0.21
5.80	1.40	1.65	0.25
5.85	2.60	3.82	1.22
5.90	6.73	8.47	1.74
5.95	11.4	15.6	4.2
6.00	19.8	24.4	4.6
6.05	27.5	29.8	2.3
6.10	33.8	36.7	2.9
6.15	42.9	47.6	4.7
6.20	55.7	62.7	7.0
6.25	74.1	75.5	1.4
6.279	100.0	100.0	0

and quintic structural parameters and uncertainties in the cubic spring constant and initial pitch. These uncertainties were allowed to propagate in a time dependent manner until an LCO or a dynamically stable solution was achieved. The stochastic algorithm consisted of building an interpolating function in the stochastic domain through sampling and the use of a multivariate B spline. Advantages of this method were that expected values were never computed or stored and 2 orders of magnitude reduction in computational time over a traditional MCS were obtained. Based on the PDFs predicted by the stochastic algorithm, a very rapid and accurate estimate of the probability of failure was obtained. A notable disadvantage of this algorithm, as with other stochastic algorithms with high order expansions, can be the rapid growth of sample size with added uncertainties to obtain convergence. Further research is required to reduce this problem of dimensionality. It should be noted that although this paper examined only the peak α as a response, the stochastic method is easily extended to examining other responses such as maximum plunge or the frequencies associated with pitch and plunge.

Acknowledgments

This project was sponsored and funded by the U.S. Air Force Research Laboratory, Air Force Research Laboratories/Air Vehicles Directorate, Wright–Patterson Air Force Base.

References

[1] Fung, Y., *An Introduction to Aeroelasticity*, Dover Pubilications, Inc., New York, 1969, pp. 160–185.

[2] Bunton, R. W., and Denegri, C. M., "Limit Cycle Oscillation Characteristics of Fighter Aircraft," *Journal of Aircraft*, Vol. 37, No. 5, Sept.–Oct. 2000, pp. 916–918.

[3] Lee, B., Jiang, L., and Wong, Y., "Flutter of an Airfoil with a Cubic Nonlinear Restoring Force," AIAA Paper 98-1725, 1998.

[4] Matsushita, H., Saitoh, K., and Gránásy, P., "Wind Tunnel Investigation of Transonic Limit Cycle Oscillation," AIAA Paper 98-1728, 1998.

[5] Tang, L., Bartels, R., Chen, P., and Liu, D., "Simulation of Transonic Limit Cycle Oscillation Using a CFD Time Marching Method," AIAA Paper 2001-1290, 2001.

[6] Beran, P., "Computation of Limit Cycle Oscillation Using a Direct Method," AIAA Paper 99-1462, 1999.

[7] Lindsley, N., Beran, P., and Pettit, C., "Effects of Uncertainty on Nonlinear Plate Aeroelastic Response," AIAA Paper 2002-1271, 2002.

[8] Melchers, R., *Structural Reliability Analysis and Prediction*, Wiley, New York, 1999.

[9] Grigoriu, M., *Stochastic Calculus: Applications in Science and Engineering*, Birkhäuser, Boston, 2002.

[10] Ibrahim, R., "Structural Dynamics with Parameter Uncertainties," *Applied Mechanics Reviews*, Vol. 40, No. 3, March 1987, pp. 309–328.

[11] Manohar, C., and Ibrahim, R., "Progress in Structural Dynamics with Stochastic Parameter Variations," *Applied Mechanics Reviews*, Vol. 52, No. 5, May 1999, pp. 177–197.

[12] Beran, P., and Silva, W., "Reduced Order Modeling: New Approaches to Computational Physics," AIAA Paper 2001-0853, 2001.

[13] Beran, P. S., and Pettit, C. L., "Prediction of Nonlinear Panel Response Using Proper Orthogonal Decomposition," AIAA Paper 2001-1292, 2001.

[14] Beran, P., and Pettit, C., "Reduced-Order Modeling for Flutter Prediction," AIAA Paper 2000-1446-CP, 2000.

[15] Pettit, C. L., and Beran, P. S., "Application of Proper Orthogonal Decomposition to the Discrete Euler Equations," *International Journal for Numerical Methods in Engineering*, Vol. 55, Oct. 2002, pp. 479–497.

[16] Ghanem, R. G., and Spanos, P. D., *Stochastic Finite Element Methods: A Spectral Approach*, Springer–Verlag, New York, 1991, Chap. 2.

[17] Ghanem, R., "A Comparative Analysis of FORM/SORM and Polynomial Chaos Expansions for Highly Nonlinear Systems," *Engineering Mechanics: Proceedings of the 11th Conference*, edited by Y. Lin and D. Ghiocel, Vol. 1, Engineering Mechanics Division of ASCE, American Society of Civil Engineers, New York, 1996, pp. 535–538.

[18] Li, R., and Ghanem, R., "Adaptive Polynomial Chaos Expansions Applied to Statistics of Extremes in Non-Linear Random Vibration," *Probabilistic Engineering Mechanics*, Vol. 13, No. 2, 1997, pp. 125–136.

[19] Le Maître, O. P., Knio, O. M., Najm, H. N., and Ghanem, R. G., "A Stochasitc Projection Method for Fluid Flow," *Journal of Computational Physics*, Vol. 173, No. 2, 2001, pp. 481–511.

[20] Xiu, D., and Karniadakis, G. E., "Modeling Uncertainty in Flow Simulations via Generalized Polynomial Chaos," *Journal of Computational Physics*, Vol. 187, No. 1, May 2003, pp. 137–168.

[21] Xiu, D., Lucor, D., Su, C.-H., and Karniadakis, G. E., "Stochastic Modeling of Flow-Structure Interactions Using Generalized Polynomial Chaos," *Journal of Fluids Engineering*, Vol. 124, March 2002, pp. 51–58.

[22] Xiu, D., and Karniadakis, G. E., "Modeling Uncertainty in Steady State Diusion Problems via Generalized Polynomial Chaos," *Computational Methods in Applied Mechanics*, Vol. 191, No. 43, 2002, pp. 4927–4948.

[23] Wiener, N., "The Homogeneous Chaos," *American Journal of Mathematics*, Vol. 60, 1938, pp. 897–936.

[24] Millman, D., King, P., and Beran, P., "Airfoil Pitch and Plunge Bifurcation Behavior with Fourier Chaos Expansions," *Journal of Aircraft*, Vol. 42, No. 2, March–April 2005, pp. 376–384.

[25] Cameron, R., and Martin, W., "The Orthogonal Development of Nonlinear Functionals in Series of Fourier-Hermite Functionals," *Annals of Mathematics and Artificial Intelligence*, Vol. 48, 1947, pp. 385–392.

[26] Chorin, A. J., "Guassian Fields and Random Flows," *Journal of Fluid Mechanics*, Vol. 63, No. 1, 1974, pp. 21–32.

[27] Crow, S. C., and Canavan, G. H., "Relationship Between a Wiener–Hermite Expansion and an Energy Cascade," *Journal of Fluid Mechanics*, Vol. 41, 1970, pp. 387–403.

[28] Millman, D. R., King, P. I., and Beran, P. S., "A Stochastic Approach for Predicting Bifurcation of a Pitch and Plunge Airfoil," AIAA Paper 2003-3515, 2003.

[29] Pettit, C. L., and Beran, P. S., "Polynomial Chaos Expansion Applied to Airfoil Limit Cycle Oscillations," AIAA Paper 2004-1695, 2004.

[30] Beran, P. S., and Pettit, C. L., "A Direct Method for Quantifying Limit Cycle Oscillation Response Characteristics in the Presence of Uncertainties," AIAA Paper 2004-1695, 2004.

[31] Le Maître, O. P., Knio, O. M., Najm, H. N., and Ghanem, R. G., "Uncertainty Propagation Using Wiener-Haar Expansions," *Journal of Computational Physics*, Vol. 197, No. 1, 2004, pp. 28–57.

[32] Le Maître, O. P., Knio, O. M., Najm, H. N., and Ghanem, R. G., "Multi-Resolution Analysis of Wiener-Type Uncertainty Propagation Schemes," *Journal of Computational Physics*, Vol. 197, No. 2, 2004, pp. 502–531.

[33] Seydel, R., *From Equilibrium to Chaos: Practical Bifurcation and Stability*, Elsevier Science Publishing Co., Inc, New York, 1988, Chap. 2.

[34] Duda, R. O., Hart, P. E., and Stork, D. G., *Pattern Classification*, 2nd ed., John Wiley and Sons, Inc., New York, 2001.

[35] de Boor, C., *A Practical Guide to Splines*, revised ed., Springer–Verlag, New York, 2001.

[36] Ghanem, R., and Spanos, P., "A Stochastic Galerkin Expansion for Nonlinear Random Vibration Analysis," *Probabilistic Engineering Mechanics*, Vol. 8, Nos. 3,4, 1993, pp. 255–264.

C. Pierre
Associate Editor